Indoor mmWave Channel Characterization with Large Virtual Antenna Arrays

Alfred Mudonhi*†‡, Raffaele D'Errico*†, Claude Oestges‡
*CEA-Leti, Grenoble, France, alfred.mudonhi@cea.fr, raffaele.derrico@cea.fr
†Universite Grenoble-Alpes, Grenoble, France
‡ICTEAM-Universite catholique de Louvain, Belgium, claude.oestges@uclouvain.be

***Abstract*—In this paper we present an indoor channel measurement campaign from 26 to 30 GHz, using a virtual antenna array. On the receiving side a 3×3 spatial grid, moving in the environment, was considered. On the transmitting side we considered a massive virtual array of 21×21 elements. Multipath components were extracted by means of a high resolution algorithm. The results obtained with the full massive array are compared with those obtained with a small sub-array, in order to investigate the effect of array size in channel modeling.**

***Index Terms*—Indoor channel, millimiter waves, massive antenna array, virtual antenna array (VAAs)**

I. Introduction

The extension of MU-MIMO (Multi-User Multiple Input Multiple Output) from adopting the classical 8 base station antennas to using hundreds of base station antennas in order to simultaneously serve *K* users within the same time-frequency resources, is what we call massive MIMO [1], [2], [3]. It is important to remark that the massiveness of massive MIMO is governed by the degree that $M > K$, with *M* being the number of base station antennas and *K* as the number of users currently being served by the base station through spatial multiplexing. The use of very many antennas in massive MIMO leads to desirable properties: provision of *asymptotically favorable propagation* by the channels and *channel hardening* [4]. Each of the *K* users who are simultaneously communicating with the base station, has its own channel. A channels offers asymptotically favorable propagation when user's channel vectors are virtually orthogonal. A significant point to take note of, is that, it is the channel directions of the considered pair (of user's channels), that become orthogonal and not the channel responses. This behaviour makes it easier for the base station to mitigate interference between the users. Consequently, the spectral efficiency is improved and it is sufficient to use simple linear combining and precoding schemes. Channel hardening alleviates the need for combating small-scale fading. Massive MIMO technology is classified into 2 types: mmWave (millimeter-Wave) massive MIMO and sub-6GHz massive MIMO. The former is deployed for small coverage areas, fewer users and situations involving low user mobility while the latter is deployed for the contrary [5]. The works presented in [6], [7] focused on sub-6GHz massive MIMO.

Some works have been presented in literature for channel modeling at millimeter waves [8], [9]. These works are often based on directional steering of directive antennas. The measurements collected are then used to obtain the omnidirectional power delay profile in order to retrieve the channel characteristics [10]. The correlation-based stochastic models (CBSMs) and geometry-based stochastic models (GBSMs) are two kinds of channel models employed in massive MIMO channel modeling [11]. As far as we are aware, mmWave massive MIMO channel modeling, still needs further investigation especially regarding the antenna and channel interaction [12]. In [13], a ray launching simulation was presented for modeling an indoor massive MIMO channel. Here we address the mmWave massive MIMO channel characteristics in an indoor environment by considering virtual arrays. In this paper, the impact of the array size on the channel characteristics is investigated. The rest of the paper is structured as follows: in Section II, the measurement campaign is presented. Section III outlines the methodology and Section IV presents the preliminary results. Section V concludes the paper.

II. Measurement Campaign

The channel measurements were performed in a laboratory room at CEA-Leti. The dimensions of the room are 7 m × 4.3 m × 2.8 m. The room is furnished with 3 tables, a chair, a metallic storage cabinet, a plastic drawer chest. Also present in the room is a channel sounder (the receiver part and the transmitter part). The room has 2 white boards on 2 of its opposite walls. It also has a large glass window on one of its 4 walls as clearly depicted in the floor plan Fig. 2(b). The measurement setup is based on a 4 port Vector Network Analyzer (VNA) and 2 automatic positioners to control antenna movements while scanning spatial grids Fig. 1(a). The instruments are controlled by an external PC. Two identical vertically polarized monopole antennas of gain 1 dBi and of operating range 26 GHz to 31.5 GHz were used in the measurement campaign. On the transmitter side, spatial grids were done in the z and y axes, forming a virtual antenna array (VAA) in the zy plane. On the receiver side, spatial grids were done in the x and y axes Fig. 1(b). With 28 GHz being the centre frequency, a grid step of 5 mm coresponding to $\frac{\lambda}{2}$ was considered on both the transmitter (TX) grid and the receiver (RX) grid. Both TX and RX antennas were at a height of 1.54 m above the ground. The floor plans showing the fixed TX position and different RX positions are shown in Fig. 2(b). We should bear in mind that the only difference

between the two channel measurements is on the number of antenna elements on the transmitting VAA.

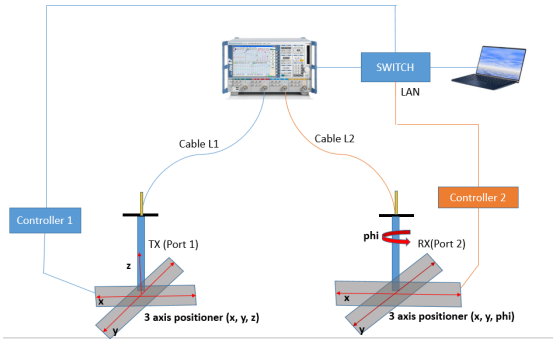

(a) Measurement setup

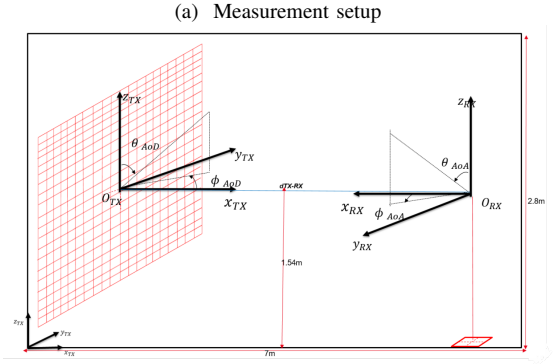

(b) Virtual arrays

Fig. 1. Picture showing the measurement setup and the virtual arrays.

(a) Measurement scenario

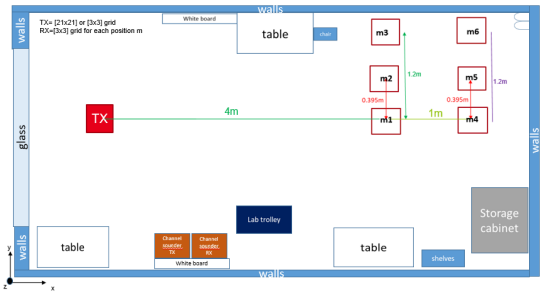

(b) Floor plan

Fig. 2. Picture showing the measurement environment and the floor plan.

III. Multipath Detection

For the multipath component detection and estimation of the channel parameters, the SAGE (Space Alternated Generalized Expectation-maximization) algorithm was implemented [14] and in particular the UWB SAGE algorithm [15]. The measured channel frequency response between one complete transmitter array spatial grid and one complete receiver array spatial grid at a particular receiver position (one of the six receiver locations) is cleaned from noise and then the SAGE algorithm is applied to the cleaned channel frequency response. Since transmit arrays are present at both sides of the communicating nodes, in this case the algorithm was used to estimate both the elevation and azimuth angles of departure and arrival. Splitting of the frequency bandwidth into subbands and implementation of the SIC (Successive Interference Cancellation) SAGE algorithm type [15] was effected in this work. The maximum number of resolvable multipath components to be estimated was set to 100.

TABLE I
VNA setup and antenna parameters.

Parameter	Value
Frequency band	26-30 GHz
Bandwidth	4 GHz
Number of sweep points	801
IF bandwidth	100 Hz
Transmitted power	10 dBm

IV. Results Discussion

A comparison between the 3×3 TX subarrays channel characteristics and the 21×21 massive TX array channel characteristics will be given. The UWB SAGE algorithm parameter settings were first verified by considering the channel transfer function measurements of the central 3×3 TX subarray. We then extracted the multipath components (MPCs) of the 21×21 massive TX array channel measurements. Considering both the 21×21 massive TX array and the central 3x3 TX subarray (of the 49, 3×3 subarrays), Fig. 3 shows the measured Power Delay Profile (PDP) and the extracted (detected) MPCs. MPCs whose power is 12 dB above the noise floor were taken into account. In Fig. 4 and Fig. 5 , we show the estimated MPCs Angle of Arrival (AoA) and Angle of Departure (AoD) as well as the MPCs' delays. Each dot correspond to a MPC, whose color is the amplitude. As expected the principal path, the LoS (Line of Sight), has an AoA / AoD close to 0° in azimuth plane and an AoA / AoD at 90° in the elevation plane. Some MPCs were detected for elevations around 50° to 70°, which most likely correspond to the reflections from the ceiling. Besides the LoS path, one can clearly distinguish other MPCs which arrive or depart at different angles, increasing the channel spread. These MPCs yield an important energy contribution that can eventually be pointed to in beamsteering when the LoS is obstructed.

A. Power delay profile

Considering the central 3×3 TX subarray measurements: for the receiver positions m1, m2 and m3 , that is the positions at the TX-RX separation distance of 4 m, the average power

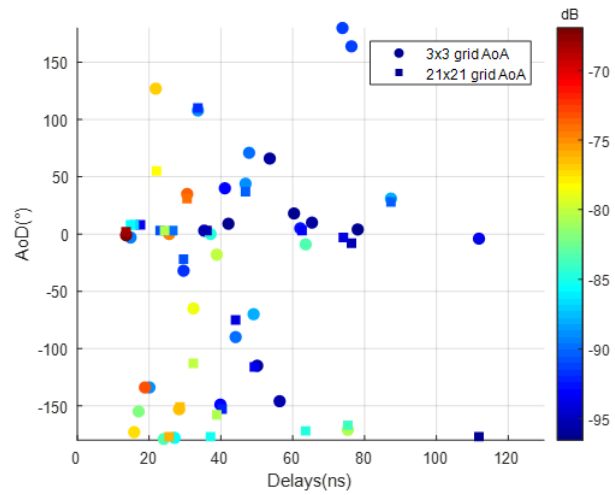

(a) Azimuth plane

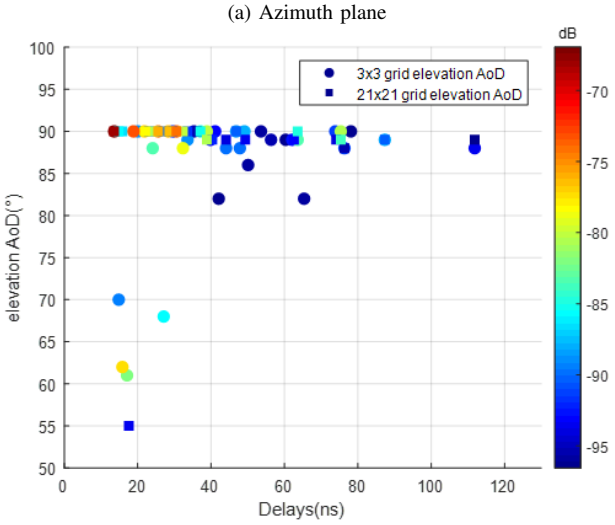

(b) Elevation plane

Fig. 5. Scatter plot: Angles of departure, 3×3 subarray vs 21×21 massive VAA.

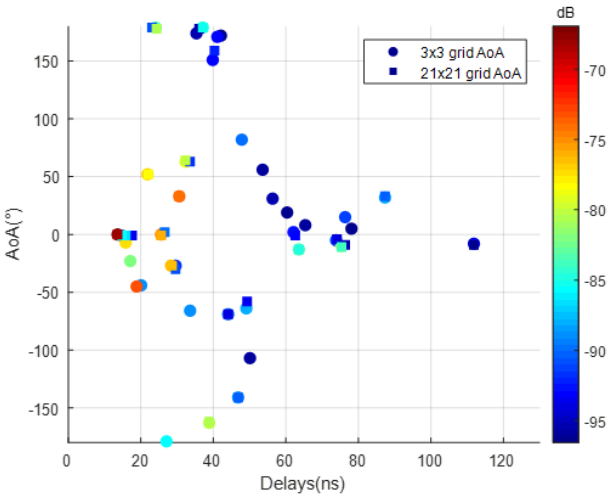

(a) Azimuth plane

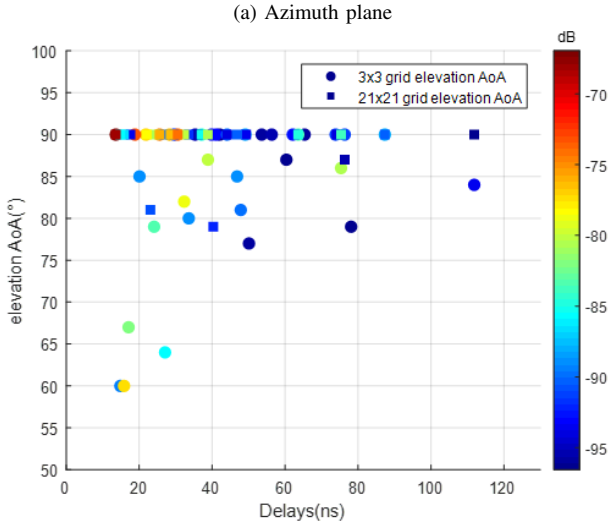

(b) Elevation plane

Fig. 4. Scatter plot: Angles of arrival, 3×3 subarray vs 21×21 massive VAA.

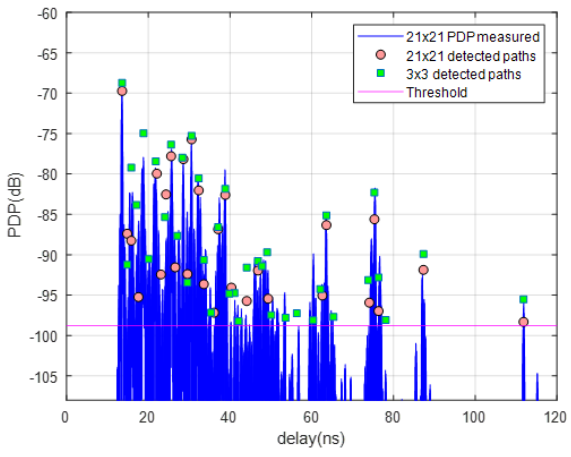

Fig. 3. Example of Measured power delay profile and the detected specular paths for one receiver grid position: 3×3 subarray vs 21×21 massive VAA.

difference between the most significant path (first path or first multipath component estimated) and the second path is 6 dB while the average power difference between the most significant path and the least significant path detected is 28.7 dB. For the TX-RX separation distance of 5 m, the corresponding values are 4.7 dB and 27.1 dB respectively. For the 21×21 massive TX array measurements: considering the receiver positions m1, m2 and m3, the average power difference between the most significant path (first path) and the second path is 6.7 dB while the average power difference between the most significant path and the least significant path detected is 21.3 dB. For the TX-RX separation distance of 5 m, the corresponding values are 8 dB and 26.5 dB respectively. In general, both measurement campaigns show that the received signal strength decreases with increasing transmitter-receiver separation distance and this is due to the extra path loss experienced by the electromagnetic waves as they propagate the extra 1 m distance.

B. Delay spread

The delay spread is inversely related to the coherent bandwidth of the channel, and it shows an overview of the delay dispersion of the multipath components arriving at the receiver. The delay spread conveys crucial information with regards to the type of fading (flat or frequency selective) the channel is subjected to. The delay spread metrics: root mean square delay spread (τ_{rms}) and the maximum delay spread τ_{max} (also known as the maximum excess delay spread) will be discussed. The former metric is obtained following (1), where τ_m, is the mean arrival delay of the multipaths and is computed using (2) . The latter metric corresponds to the difference between the longest and the shortest delays of the detected paths.

$$\tau_{rms} = \sqrt{\frac{\sum_{l=1}^{L} (\tau_l - \tau_m)^2 \alpha_l^2}{\sum_{l=1}^{L} \alpha_l^2}} \tag{1}$$

where τ_m is the mean arrival delay of the multipaths and is computed as follows:

$$\tau_m = \sqrt{\frac{\sum_{l=1}^{L} \alpha_l^2 \tau_l}{\sum_{l=1}^{L} \alpha_l^2}} \tag{2}$$

L, α_l^2 and τ_l are the number of detected multipath components, the power of the l^{th} path and the arrival delay of of the l^{th} path respectively. Table II and Table III show the different channel parameters obtained where DS is the τ_{rms} delay spread. In both measurement campaigns, the τ_{rms} delay spread increases as the the transmitter-receiver separation distance increases. This increase in delay spread values is due to the time taken by the signals in traversing the extra distance (1 m in this case).

The average τ_{max} for the positions m1, m2, and m3 is 106 ns in the central 3×3 TX subarray measurements. For the positions m4, m5 and m6 it was found to be 107 ns. The respective values for the 21×21 massive TX virtual array measurements are 90.4 ns for positions m1, m2, and m3 and 99.3 ns for positions m4, m5 and m6.

C. Angular spread

The angular spread φ_{rms}, an important parameter in MIMO systems, shows the degree of space selectivity. Typically, large angle spreads support spatial multiplexing and antenna diversity schemes which in turn lead to increased channel capacity. On the other hand, small angle spreads enable efficient beamforming technology [16]. The root mean square angular spread is obtained from (3), where φ_m is the mean arrival or departure angle of the multipath and is calculated following (4). Results for both the elevation and azimuth planes angular spreads will be discussed.

$$\varphi_{rms} = \sqrt{\frac{\sum_{l=1}^{L} (\varphi_l - \varphi_m)^2 \alpha_l^2}{\sum_{l=1}^{L} \alpha_l^2}} \tag{3}$$

$$\varphi_m = \sqrt{\frac{\sum_{l=1}^{L} \alpha_l^2 \varphi_l}{\sum_{l=1}^{L} \alpha_l^2}} \tag{4}$$

L, α_l^2 and φ_l are the number of detected multipath components, the power of the l^{th} path and the angle of arrival or departure of the l^{th} path respectively. Table II and Table III show the different channel parameters obtained. ASA and ASD are the azimuth spread of arrival and azimuth spread of departure respectively. Likewise, ZSA and ZSD are the zenith spread of arrival and zenith spread of departure, respectively. The lower angular spread values in the elevation plane compared to the azimuth plane, can be attributed to the behaviour of the monopole antenna in the elevation plane (it has its highest gain at 90° in the elevation plane hence most of the signal reception or emission is around 90°). In the azimuth plane, higher angular spread values are observed. These higher angular spread values in the azimuth plane, can be explained by the fact that the considered indoor environment is not very spacious and has a lot of scatterers. On top of the aforementioned reasons for the higher angular spread values, the monopole antenna has an omnidirectional pattern in the azimuth plane, so basically there is not a favourite direction where most of the reception or emission can take place.

TABLE II
3×3 SUB-ARRAY TX CHANNEL PARAMETERS.

Position	**m1**	**m2**	**m3**	**m4**	**m5**	**m6**
Number of paths	38	35	39	38	44	39
LoS path AOA [°]	0	6	19	1	6	15
LoS path AOD [°]	-1	-173	-161	1	-175	-164
LoS path EOD [°]	90	90	90	90	90	90
LoS path EOD [°]	90	90	90	90	90	80
LoS path path power [dB]	-67	-68.3	-67.8	-72.1	-71.4	-71.6
LoS path Delays [ns]	13.6	13.6	14.3	17.3	17.3	17.8
DS [ns]	13.2	13.8	12	16.6	14.4	10.9
ASA [°]	140	132	108	136	137	113
ASD [°]	131	43	66	72	64	71
ZSA [°]	7	10	11	5	6	4
ZSD [°]	7	10	11	5	7	7

TABLE III
21×21 MASSIVE TX ARRAY CHANNEL PARAMETERS.

Position	**m1**	**m2**	**m3**	**m4**	**m5**	**m6**
Number of paths	28	26	25	32	32	31
LoS path AOA [°]	0	6	19	1	6	15
LoS path AOD [°]	2	-4	-163	2	-178	-167
LoS path EOD [°]	90	90	90	90	90	90
LoS path EOD [°]	90	90	90	90	90	90
LoS path path power [dB]	-68	-69.4	-69	-73	-72.2	-72.6
LoS path Delays [ns]	13.6	13.6	14.3	17.3	17.6	17.8
DS[ns]	12.4	13.7	10.3	15.1	13.3	9.5
ASA[°]	137	147	82	133	129	118
ASD [°]	87	67	69	120	87	54
ZSA [°]	4	9	10	4	2	2
ZSD [°]	2	8	11	4	1	2

D. Number of detected paths

The number of detected paths also tends to increase with the transmitter-receiver separation distance. This can be attributed to the signals reflected by the walls and the roof, which initially were missing the receiver, but now can be received effectively at a further distance. Fig. 6 shows the number of MPCs extracted when considering the 21×21 massive TX array, the central 3×3 TX subarray, and the average of all the 49, 3×3 TX subarrays. Generally the number of MPCs is lower when considering high number of antennas. This could be explained by the fact that SAGE is based on small-signal variation hypothesis. It means that the only phase difference on MPCs phase is due to the geometrical shift of the antenna within the array. However, considering the relative short distances in the considered indoor scenario, this could not be verified anymore. This explanation is also verified by the fact that the number of MPCs is not constant when considering the 49, 3×3 subarrays, which results into the fact that different portion of the massive array do not see the same channel.

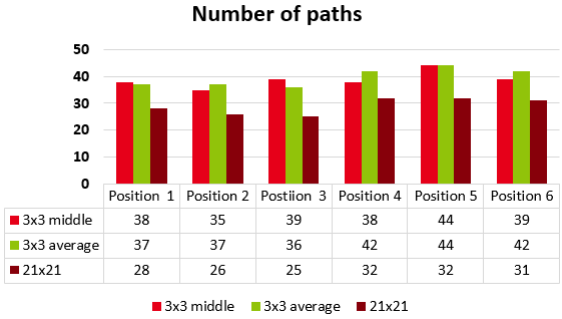

Fig. 6. Number of MPCs considering different array size.

V. Conclusion

A measurement campaign using virtual antenna arrays has been presented in this paper. Preliminary results of the measurement campaign show that the estimation of the LoS path is almost unchanged when considering a massive array or a subarray. On the contrary, the size of the array has an impact on the secondary multipath component estimation. Despite the fact that the energy contribution of the secondary MPCs is relatively small, this difference yields to different overall delay and angular estimations. When considering different subarrays in the massive MIMO array, the results suggest that different MPCs are seen by the array. As a next step, the variation of the MPCs as seen from one subarray to another will be investigated.

Acknowledgment

This work was partially funded by the 5GmmFlash project and the MOREOVER project.

References

[1] T. L. Marzetta, Noncooperative Cellular Wireless with Unlimited Numbers of Base Station Antennas. IEEE Transactions on Wireless Communications 9.11 (2010): 35903600.

[2] T. L. Marzetta, "Massive MIMO: an introduction" in Bell Labs Technical Journal, 20, 11-22, 2015.

[3] E. Bjrnson, E. G. Larsson and T. L. Marzetta, "Massive MIMO: ten myths and one critical question," in IEEE Communications Magazine, vol. 54, no. 2, pp. 114-123, February 2016.

[4] H. Q. Ngo, E.G. Larsson and T.L. Marzetta, "Aspects of favorable propagation in Massive MIMO," 2014 22nd European Signal Processing Conference (EUSIPCO), Lisbon, pp. 76-80, 2014.

[5] E. Bjrnson, J. Hoydis, and L. Sanguinetti, "Massive MIMO networks: Spectral, energy, and hardware efficiency", Foundations and Trends in Signal Processing, 11(3-4), 154-655, 2017.

[6] E. G. Larsson, O. Edfors, F. Tufvesson, and T. L. Marzetta, " Massive MIMO for next generation wireless systems", IEEE communications magazine, 52(2), 186-195, 2014.

[7] S. Payami, and F. Tufvesson, "Channel measurements and analysis for very large array systems at 2.6 GHz", in 2012 6th European Conference on Antennas and Propagation (EUCAP) (pp. 433-437),IEEE, March, 2012.

[8] A. Bamba, F. Mani and R. DErrico, "Millimeter-Wave Indoor Channel Characteristics in V and E Bands," in IEEE Transactions on Antennas and Propagation, vol. 66, no. 10, pp. 5409-5424, Oct. 2018.

[9] M. K. Samimi, S. Sun, and T. S. Rappaport, "MIMO channel modeling and capacity analysis for 5G millimeter-wave wireless systems" in 2016 10th European Conference on Antennas and Propagation (EuCAP) (pp. 1-5).IEEE, April 2016.

[10] K. Haneda, S. L. H. Nguyen, J. Jrvelinen and J. Putkonen, "Estimating the omni-directional pathloss from directional channel sounding," 2016 10th European Conference on Antennas and Propagation (EuCAP), Davos, 2016, pp. 1-5.

[11] K. Zheng, S. Ou, and X. Yin, "Massive MIMO channel models: A survey" in International Journal of Antennas and Propagation, 2014.

[12] S. Mumtaz, J. Rodriguez, and L. Dai, "MmWave Massive MIMO: A Paradigm for 5G" in Academic Press, 2016.

[13] J. Weng, X. Tu, Z. La, S. Salous, and J. Zhang, "Indoor massive MIMO channel modelling using ray-launching simulation" in International Journal of Antennas and Propagation, 2014.

[14] B. H. Fleury D. Dahlhaus R. Heddergott M. Tschudin, "Wideband angle of arrival estimation using the SAGE algorithm" Proc. IEEE Fourth Int. Symp. Spread Spectrum Techniques and Applications (ISSSTA '96) pp. 79-85 September 1996.

[15] K. Haneda, and J. I. Takada, " An application of SAGE algorithm for UWB propagation channel estimation" in IEEE Conference on Ultra Wideband Systems and Technologies,(pp. 483-487), November 2003.

[16] M. Juha, et al. "D5. 3: WINNER+ final channel models " in Wireless World Initiative New Radio WINNER (2010).